Electronic structure and topology across T_c in the magnetic Weyl semimetal $Co_3Sn_2S_2$

Antonio Rossi,[1,2,*] Vsevolod Ivanov,[1,*] Sudheer Sreedhar,[1] Adam L. Gross,[1] Zihao Shen,[1] Eli Rotenberg,[2]
Aaron Bostwick,[2] Chris Jozwiak,[2] Valentin Taufour,[1] Sergey Y. Savrasov,[1] and Inna M. Vishik[1,†]
[1]*Department of Physics and Astronomy, University of California, Davis, California 95616, USA*
[2]*Advanced Light Source, Lawrence Berkeley National Lab, Berkeley, California 94720, USA*

(Received 18 May 2021; revised 1 August 2021; accepted 24 September 2021; published 11 October 2021;
corrected 2 November 2021)

$Co_3Sn_2S_2$ is a magnetic Weyl semimetal, in which ferromagnetic ordering at 177 K is predicted to stabilize Weyl points. We perform temperature and spatial dependent angle-resolved photoemission spectroscopy measurements through the Curie temperature (T_c), which show large band shifts and renormalization concomitant with the onset of magnetism. We argue that $Co_3Sn_2S_2$ evolves from a Mott ferromagnet below T_c to a correlated metallic state above T_c. To understand the magnetism, we derive a tight-binding model of Co-$3d_{x^2-y^2}$ orbitals on the kagome lattice. At the filling obtained by first-principles calculations, this model reproduces the ferromagnetic ground state, and results in the reduction of Coulomb interactions due to cluster effects. Using a disordered local moment simulation, we show how this reduced Hubbard U leads to a collapse of the bands across the magnetic transition, resulting in a correlated state, which carries associated characteristic photoemission signatures that are distinct from those of a simple lifting of exchange splitting. The behavior of topology across T_c is discussed in the context of this description of the magnetism.

DOI: 10.1103/PhysRevB.104.155115

I. INTRODUCTION

Quantum materials encompass a broad array of phenomena, unified by the concept of emergent phases [1,2], which can arise as result of thermodynamic or topological phase transitions. Recently, magnetic topological materials have united these two paradigms with a promise to realize novel elementary excitations in a switchable manner, as exemplified by magnetic Weyl semimetals (WSMs). Magnetic WSM states were initially predicted in rare-earth pyrochlore iridates [3], and $HgCr_2Se_4$ [4], and recently observed in a number of materials [5–9].

A WSM state occurs as an intermediate metallic regime between normal and topologically insulating phases when either inversion ($\mathcal{I}$) or time-reversal ($\mathcal{T}$) symmetries are broken [10–12]. Specifically, magnetic WSMs break $\mathcal{T}$ symmetry, and can realize the minimal number of Weyl points in the Brillouin zone (BZ), since the preserved inversion symmetry guarantees the existence of Weyl points with opposite chirality at $\boldsymbol{k}/-\boldsymbol{k}$ momenta, necessarily satisfying the Nielsen-Ninomiya theorem [13]. This chirality is topological property that manifests as Fermi arc surface states [3,10] connecting pairs of projected Weyl points, and generally guarantees their stability, since the chirality can only be removed by merging with a Weyl point of opposite chirality.

A prototype magnetic WSM is $Co_3Sn_2S_2$, which is a ferromagnet with a Curie temperature of $T_c = 177\,\mathrm{K}$ [14,15]. The structure is composed of triangular S and Sn layers interspersed between the kagome lattice planes of Co atoms that are responsible for ferromagnetic order. This material possesses an unusually large anomalous Hall conductivity as a direct consequence of its topological band structure [16,17]. Other indications of the topology in $Co_3Sn_2S_2$ are the chiral anomaly-related negative longitudinal magnetoresistance [16] and gigantic magneto-optical response [18]. The topological nature of the band structure has been verified spectroscopically at low temperature [19–21], but limited spectroscopic information is available through T_c [22,23].

Switchable topology in magnetic WSMs has been implied through various experiments, including measurements of the intrinsic anomalous Hall [4,16,24–26] and Nernst effects [27–29], but direct signatures of band structure changes across T_c have been less explored. This is in part because the microscopic details of magnetism can be quite complex [22,30–34], resulting in a nonobvious evolution of the band structure and its topological features. The topological physics of $Co_3Sn_2S_2$ is simultaneously manageable due to it only possessing six Weyl points, the minimum allowed by the combined $\mathcal{I}$ and C_3 symmetries, yet is still highly nontrivial because its magnetic structure is complicated by correlations [22,30,32], frustrations [33,34], and domains [31]. These aspects make this material a convenient experimental platform for observing an elementary property of WSM: The merging and annihilation of Weyl points with opposite chirality across a magnetic phase transition [35,36]. Studying this theoretically predicted topological property of Weyl points holds not only pedagogical importance, but is also a crucial step towards controlling and manipulating electronic states in this system.

---

[*] These authors contributed equally to this work.
[†] ivishik@ucdavis.edu

In the present paper, we investigate the evolution of electronic structure across T_c in magnetic WSM $Co_3Sn_2S_2$ using spatial and temperature-dependent angle-resolved photoemission spectroscopy (ARPES) and corresponding first principles calculations. Our ARPES measurements reveal a substantial band shift and renormalization across T_c, as well as a second band farther from the Fermi energy. We draw an analogy from the well-known Mott-Hubbard physics, explaining this result as the emergence of a moderately correlated metallic state above T_c, characterized by a distinctive renormalized quasiparticle band near the Fermi energy, with the persistent spectral weight attributed to the remnants of the lower Hubbard band. To better understand the evolution across T_c, we perform calculations based on the disordered local moment (DLM) [37] picture of magnetism to show how persisting local magnetic correlations can lead to a renormalized quasiparticle band. We then show that the states associated with the bulk Weyl nodes and Fermi arcs are absent above T_c, consistent with the reappearance of $\mathcal{T}$ symmetry. However, in our proposed model the persistent local moments above T_c may also break the translational symmetry required for Weyl nodes to exist, oppugning the notion that they annihilate across the magnetic transition, and emphasizing the crucial role played by many-body effects during the evolution of magnetism and topology across T_c.

This paper is organized as follows: In Sec. II we discuss the magnetism of $Co_3Sn_2S_2$, and derive a minimal tight binding model, while Sec. III focuses on understanding the surface terminations of $Co_3Sn_2S_2$. The remainder of the paper illustrates the changes in the band structure on the Sn termination across T_c, by considering the magnetic disorder and topological features in this material. In Sec. IV, the derived tight binding model is used in combination with first-principles disordered local moment simulations to understand the ARPES data across T_c. Section V then depicts the evolution of bulk Weyl cones across the magnetic transition, and uses the results of slab calculations to describe how the associated Fermi arc states will evolve.

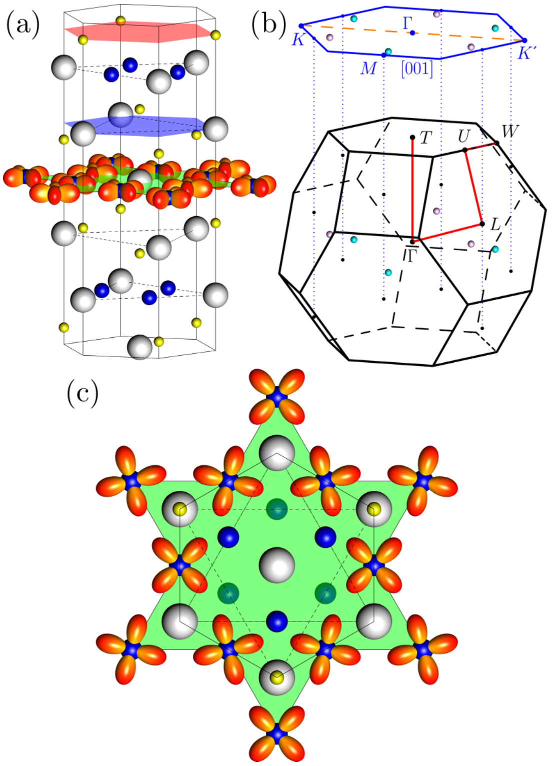

FIG. 1. Structure and BZ of $Co_3Sn_2S_2$. (a) Shandite-type crystal structure of Co (blue), Sn (white), and S (yellow) atoms. Colored planes mark the S-type (red), Sn-type (blue) terminations, and Co kagome sublattice (green). (b) BZ and projection along [001], with high-symmetry points indicated. Dashed-orange line on the two-dimensional projection shows the high-symmetry $\Gamma - K$ cut. Pink/cyan spheres mark Weyl points in the BZ and their surface projections. (c) Kagome plane Co-$3d_{x^2-y^2}$ orbitals (red), rotated by $-\pi/12$, $\pi/12$, or $\pi/4$, to align with local C_3 cluster symmetry.

II. MECHANISM OF MAGNETIC ORDER

$Co_3Sn_2S_2$ crystallizes in the hexagonal shandite-type structure [38–42] with A-B-C stacking in the [001] direction (space group $R\bar{3}m$, #166), shown in Fig. 1(a). The layers alternate as...-Sn-[S-(Co_3-Sn)-S]-... units, with the Sn layer and Co_3-Sn layer separated by sulfur atoms. The Co atoms form a Kagome lattice with Sn atoms positioned at the center of each hexagon [Fig. 1(c)].

Magnetic order in this compound has been extensively characterized by experiments [14,15,43–45]. Below T_c, $Co_3Sn_2S_2$ exists in a ferromagnetic phase, with a local moment of $\sim 0.33\,\mu_B$/Co atom along the easy magnetization c axis. Recent experiments have also suggested the existence of an anomalous magnetic phase just below the transition temperature [32,34,46]. Within the ferromagnetic phase, broken $\mathcal{T}$ symmetry leads to the formation of Weyl points just above the Fermi energy. This band structure topology has been verified through measurements of the spectroscopy [19–21], anomalous Hall conductivity [16,17], anomalous Nernst conductivity [27], negative longitudinal magnetoresistance [16], and gigantic magneto-optical response [18].

The magnetic order of $Co_3Sn_2S_2$ is understood from previous electronic structure calculations as follows [15,47]. The spin-minority channel develops a gap structure, leaving a Fermi surface composed exclusively of spin-majority states, which makes $Co_3Sn_2S_2$ a half-metallic ferromagnet. The states at the Fermi level are comprised primarily of Co-$3d$ orbitals, but there is no consensus on the precise magnetic orbital(s) nor mechanism, with various works proposing minimal tight-binding models that assign the magnetism to Co-d_{z^2} [48], Co-$J_{1/2}$ [49], or Co-$3d$-e_g [50]. However, the standard approach is to extract a tight-binding model directly from the electronic structure calculation, by projecting onto a basis of maximally localized Wannier functions [19,25,45,49,51]. Nevertheless, this procedure is cumbersome and necessitates an excess of orbital fitting parameters in order to adequately reproduce the electronic bands. The large number of Wannier orbitals needed for most fits, and the possibility of fitting bands with the wrong orbitals, makes it difficult to analyze the electronic structure and physics of complex materials.

To understand the origin of the magnetism in $Co_3Sn_2S_2$, we employ the full-potential linear muffin-tin orbital (FPLMTO) method [52,53] to perform density functional theory

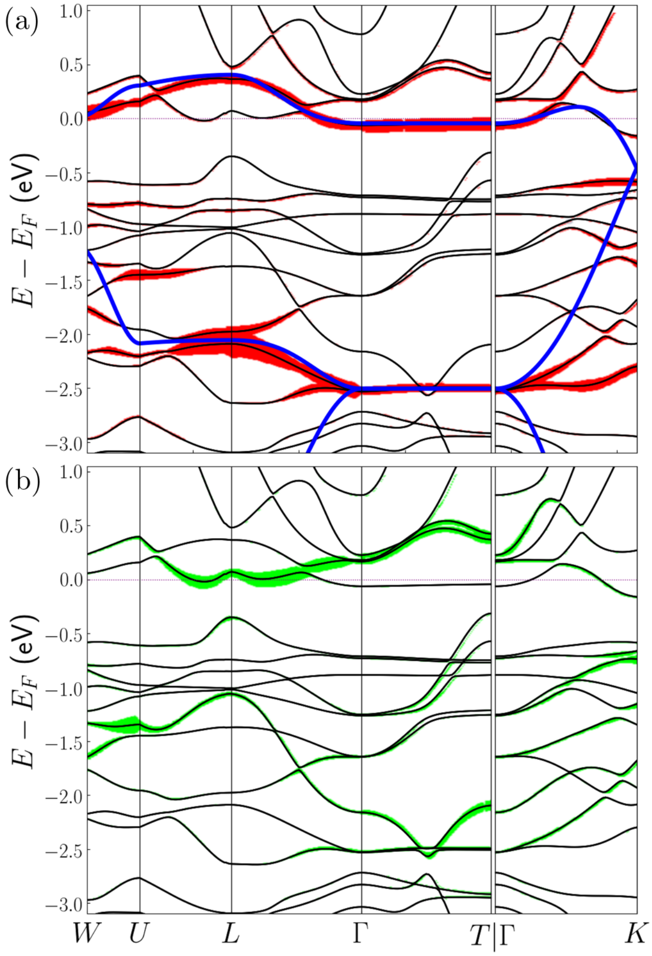

FIG. 2. LDA band structure of $Co_3Sn_2S_2$. The orbital characters for the Co-3d basis, rotated about k_z by $-\pi/12$, $\pi/12$, and $\pi/4$, are highlighted red for $d_{x^2-y^2}$ (a) and green for d_{z^2} (b). The $d_{x^2-y^2}$ tight-binding model bands are shown in blue.

calculations. The electronic structure is computed within the local density approximation (LDA), local spin density approximation (LSDA), and with the Hubbard-U correction included (LDA+U) to take into account the electron-electron interactions on the Co-3d orbitals. In order to best match experimental results, the parameter U is varied from $U = 2-4$ eV and with Hund's $J_H = 0.8$, in accordance with recent many-body simulations [30].

The LDA electronic structure calculation reveals two bands crossing the Fermi energy (Fig. 2), carrying mainly Co-3d character. To obtain a clearer picture, we project onto a basis set of cubic harmonics that are rotated about the k_z axis by $-\pi/12$ for Co-1, $+\pi/12$ for Co-2, and $+\pi/4$ for Co-3, which respects the local C_3 rotational symmetry and aligns the orbitals with the in-plane nearest-neighbor Co bonds [Fig. 1(c)]. In this new basis, the two bands crossing the Fermi level have $d_{x^2-y^2}$ character for the half-filled flat band that dips below E_F along $\Gamma - T$, and d_{z^2} character for the other, mostly unoccupied band. Below E_F, the dispersion of local $d_{x^2-y^2}$ orbitals [red-fat lines in Fig. 2(a)] is more complicated due to hybridization with many other bands, which can be seen within a large energy window from –2.5 eV to –0.5 eV.

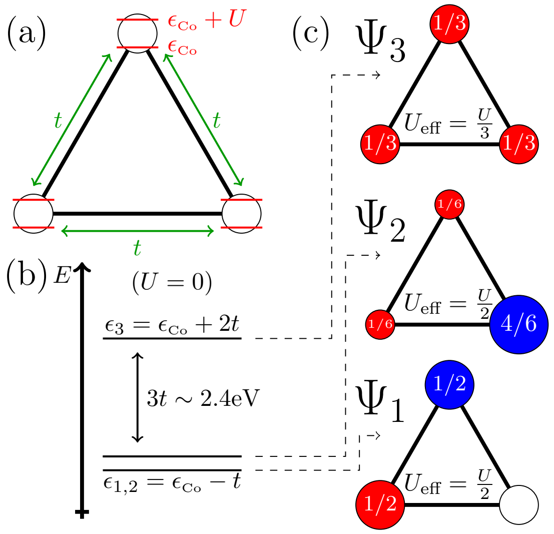

FIG. 3. (a) Local Hubbard model on the three Co atom cluster. Diagonalizing the noninteracting case yields a pair of degenerate states and one higher energy state (b), with the probability density distributions shown in (c). Coulomb interactions are screened for Ψ_3, yielding $U_{\rm eff} = U/3$.

The lack of dispersion along $\Gamma - T$ for the Co-$d_{x^2-y^2}$ band implies that the electron hoppings are confined within the kagome plane. It is well known that a tight-binding model restricted to only include nearest-neighbor in-plane hoppings produces an ideally flat band [45]. For the case of the band structure here, we see some additional dispersion along $U - L - \Gamma$, which suggests higher order hoppings. Indeed the band structure can be closely reproduced (Fig. 2) by including couplings up to third order as shown in the Supplemental Material (SM) [54], with on-site energy $\epsilon_{\rm Co} = -1.87$ eV, and hoppings $t_1 = 0.77$ eV, $t_2 = -0.36$ eV, and $t_3 = 0.046$ eV. These parameters are similar to those used for tight-binding models in previous works [48,49], notwithstanding the different basis sets that were employed.

The basic structure of the energy bands can be illustrated by considering what happens locally on a triangular Co atom cluster (Fig. 3), with $\psi_{\rm Co1}$, $\psi_{\rm Co2}$, $\psi_{\rm Co3}$ forming the basis of orbitals on the three Co atoms. Considering only on-site and nearest-neighbor hoppings in the noninteracting picture yields the 3×3 Hamiltonian

$$\mathcal{H} = \begin{pmatrix} \epsilon_{\rm Co} & t_1 & t_1 \\ t_1 & \epsilon_{\rm Co} & t_1 \\ t_1 & t_1 & \epsilon_{\rm Co} \end{pmatrix}, \qquad (1)$$

which can be diagonalized to find the eigenstates $\Psi_1 = (-\psi_{\rm Co1} + \psi_{\rm Co2})/\sqrt{2}$, $\Psi_2 = (\psi_{\rm Co1} + \psi_{\rm Co2} - 2\psi_{\rm Co3})/\sqrt{6}$, and $\Psi_3 = (\psi_{\rm Co1} + \psi_{\rm Co2} + \psi_{\rm Co3})/\sqrt{3}$. $\Psi_{1,2}$ form a doubly degenerate ground state with energy $\epsilon_{1,2} = \epsilon_{\rm Co} - t_1$, lying below Ψ_3, which has an energy $\epsilon_3 = \epsilon_{\rm Co} + 2t_1$.

We now diagonalize this model with an on-site Coulomb repulsion U, and consider what happens for different electron fillings. At half-filling the two lowest energy configurations are: $S = 1/2$ with all three electrons in the lower energy doublet, and the higher energy $S = 3/2$ where one electron occupies Ψ_3. Adding an additional electron preferentially fills the hole in the doublet, resulting in a $S = 0$ ground state and $S = 0, 1$ excited configuration. At a filling of 5/6 electrons the situation is simplified; the lowest energy configuration matches the single electron picture with the solitary hole occupying Ψ_3, which corresponds to $S = 1/2$.

This in fact matches what is seen in LDA calculations; the highest-lying $d_{x^2-y^2}$ band is half filled, in line with a five electron/one hole configuration. This results in a spin-1/2 ferromagnetic state, since the antiferromagnetic state is impeded by lattice frustration. The associated moment of 1 μ_B is spread over the Co atoms in the Ψ_3 state, consistent with the 0.33 μ_B per Co magnetic moment computed by LSDA. The experimentally measured moment is slightly less than 1 μ_B/f.u. [15,43,54], due to the partial filling of the d_{z^2} band.

The Ψ_3 state is optimal from the standpoint of minimizing Coulomb repulsion. For Ψ_1 and Ψ_2 the Coulomb repulsion is slightly reduced to $U/2$, while the symmetric distribution for Ψ_3 results in a net repulsion of $U/3$. Considering a range $U \sim 2-4$ eV, which is typical for Co atoms in magnetic systems, the electron filling up to the half-filled Ψ_3 state reduces this to values comparable with the bandwidth (Fig. 2) found by first-principles calculations (as shown in the SM [54]). This means that the disordered magnetic phase near T_c (to be considered in a later section), is a true strongly correlated state, and must be treated appropriately. Recent single-impurity DMFT simulations were not able to fully capture the electronic-bandwidth renormalization [30]. Thus a complete treatment would entail a calculation that captures the full physics of the three-Co-atom clusters, through a method such as cluster-DMFT [55]. Such an approach is outside the scope of the present paper, but may yield important insights in the future.

III. SURFACE TERMINATIONS

From a theory standpoint, the presence of Weyl points in the bulk guarantees the existence of topological Fermi arcs on the surface [3,10], but the shape and connectivity of these arcs have been shown to critically depend on surface termination [56]. $Co_3Sn_2S_2$ cleaves by breaking either Co–S or Sn–S bonds, with the latter being more probable [51], making Sn and S the dominant terminations. These cleave terminations in $Co_3Sn_2S_2$ have implications for Fermi arc connectivity, resulting in *intra*-BZ Fermi arcs on the Sn termination, *inter*-BZ Fermi arcs on the Co termination [19], and very short Fermi arcs on the S termination due to mixing with bulk states [51]. Additionally, the S termination is susceptible to vacancy formation, and these vacancies themselves yield novel excitations [57,58]. As such, identifying the photoemission fingerprints of different terminations is crucial for the study of temperature-dependent band structure and topology.

Photoemission experiments were performed at beamline 7.0.2 (MAESTRO) at the Advanced Light Source (ALS), with a beam spot size $d \approx 80\,\mu$m. 115-eV photon energy was used for ARPES measurements, which accesses near the Γ plane of the BZ and has been shown to cut through Weyl points [20]. X-ray photoemission spectroscopy (XPS) with 350 eV photon energy was used to assess core levels at each measured sample position.

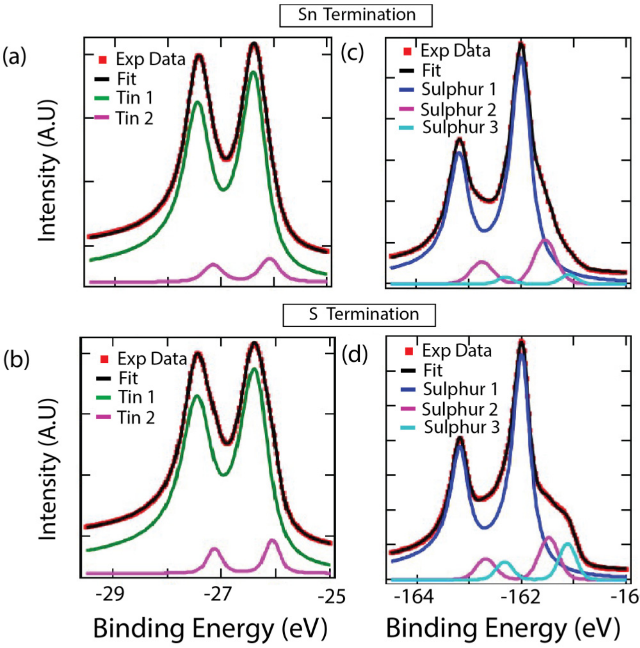

FIG. 4. Sn and S core levels on different surface terminations. [(a),(b)] Sn *4d* core level spectra taken on portions of the sample with Sn (a) and S (b) terminations. Core levels are fitted with two DS doublets in order to represent the contribution from the first two Sn layers. [(c), (d)] S *2p* core level spectra at the same positions of the sample with Sn (c) and S (d) terminations fitted with three DS doublets representing the contribution from the first three S layers. All spectra taken at 30 K.

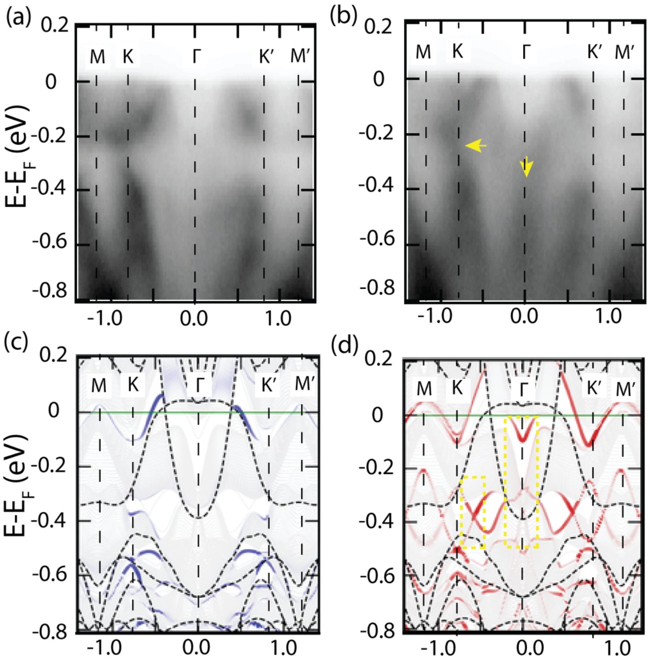

FIG. 5. High symmetry $\Gamma - K$ cuts taken at 30 K for Sn (a) and S (b) terminations. Arrows point to features near Γ and K, which differ between the two terminations. [(c), (d)] Slab calculations along $M - K - \Gamma - K' - M'$. Dashed lines indicate bulk bands. Slab bands are colored based on surface character: blue, Sn termination; red, S termination; grey, bulk. Vertical dashed lines mark high symmetry points throughout.

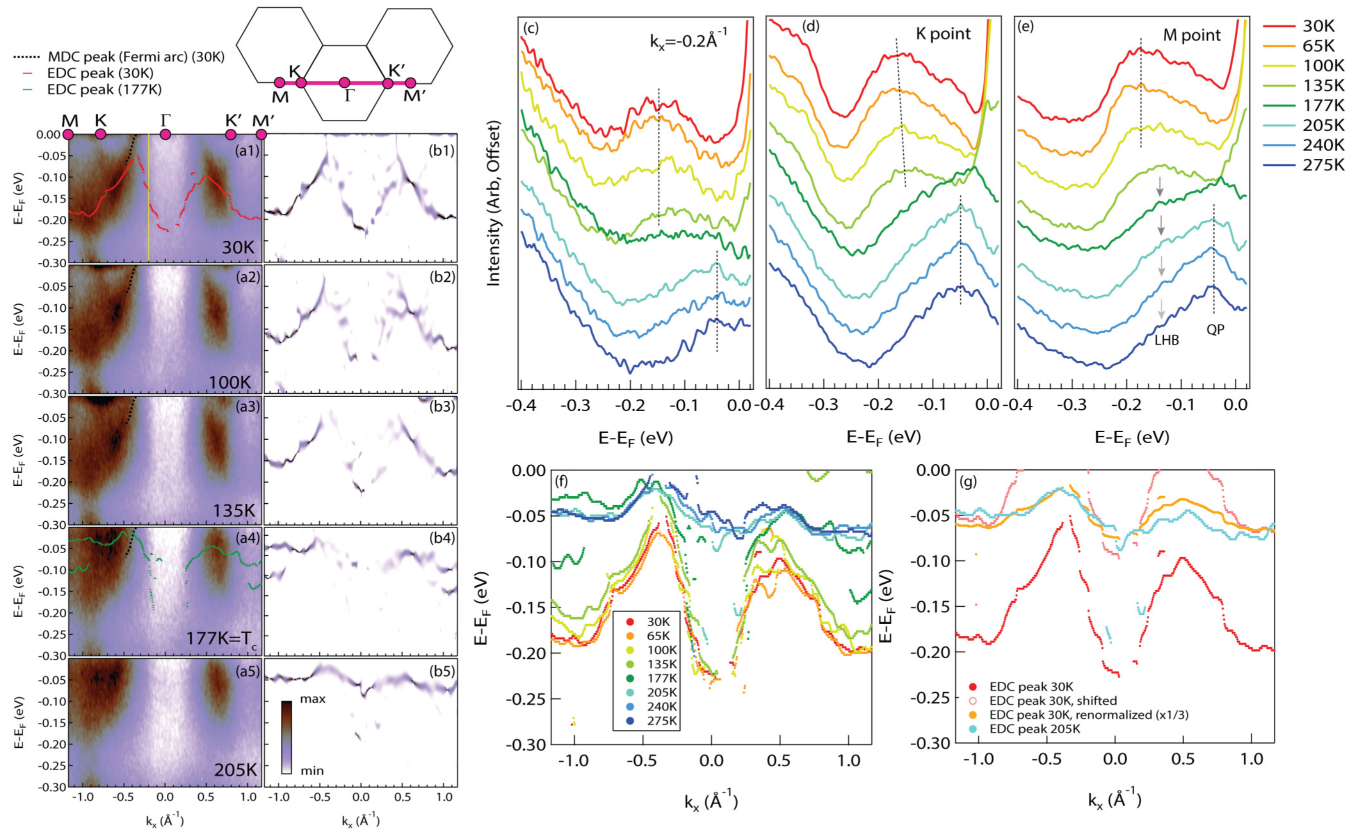

FIG. 6. Temperature dependence of the $\Gamma - K$ cut. (a) Selected temperatures along cut indicated in schematic above panels. In all spectra, a Fermi-Dirac cutoff convolved with the energy resolution has been divided out. Black dashed line indicates position of band, which forms Fermi arc, as quantified by MDC fitting at 30 K. The same dispersion is plotted in (a1)–(a4). (b) corresponding curvature plots [65] at each temperature; [(c)–(e)] temperature-dependent EDCs at $k_x = 0.2$, K point, and M point, respectively. Curves normalized at $E_B = 1$ eV and offset for clarity. Dashed lines are guide-to the eye for EDC peak position in each panel, and grey arrows in (e) are guide-to-the-eye for high-energy shoulder. LHB and QP label the lower Hubbard and quasiparticle bands, as discussed in text. All EDCs have Fermi-Dirac function divided out. (f) EDC local maxima at each studied temperature. (g) Comparison of band positions as quantified by EDC local maxima at 30 K ($<T_c$) and 205 K ($>T_c$). A rigid band shift by 130 meV is contrasted with renormalization by 1/3 for comparison with 205 K data.

Figures 4 and 5 show results for the two surface terminations realized at different positions in our $Co_3Sn_2S_2$ samples. These are identified as Sn and S surfaces, respectively, indicated by the blue and red planes in Fig. 1. The most probable identity of the termination in different positions on the same sample is determined from density functional theory (DFT) calculations, which are presented later. These different terminations are most readily distinguishable by their S $2p_{1/2,3/2}$ core level spectra shown in Figs. 4(a) and 4(b), which display an extra low-energy shoulder on the S termination [Fig. 4(b)]. Sn $4d_{3/2,5/2}$ core levels were also measured Figs. 4(c)–4(d)], and do not show as visually apparent differences as a function of termination. XPS spectra were fitted to Doniach-Sunjic (DS) doublet profiles with a Shirley background. Three sets of doublets are needed to fully capture the S core levels: one associated with bulk states and two associated with two near-surface sulfur layers. The latter contribute more strongly on the S termination, producing the characteristic shoulder. Sn core levels were fitted to two DS doublets, but have only subtle lineshape differences at different cleave terminations.

Having established the presence of two distinct surface terminations, we now turn to the measured and calculated band structure at the same positions as the XPS spectra. Figures 5(a) and 5(b) show ARPES spectra along the $\Gamma - K$ high-symmetry direction for Sn (a) and S (b) terminations. The cut extends into the second BZ, and high symmetry points are labeled. Low energy features, which are most relevant to magnetism and topology along this high-symmetry cut are discussed in Fig. 6 and SM [54]. Here, we focus on characteristic differences between the two cleave terminations. The most prominent spectral changes appear at the Γ point [vertical yellow arrow in Fig. 5(b)] and also at $k_x \approx 0.8$ Å^{-1} near the K point [horizontal yellow arrow in Fig. 5(b)]. At the Γ point, a "Y-shaped" feature is prominent on the S termination [Fig. 5(b)], and significantly diminished on the Sn termination [Fig. 5(a)]. Meanwhile, on the Sn termination, there is a gap or depletion of spectral weight near the K point, at a binding energy $E_B \sim 300$ meV, which is more filled in on the S termination.

In order to interpret the position-dependent ARPES spectra, we extract a model Hamiltonian from the *ab initio* calculation to solve on a layered slab geometry using the following procedure. We use the Quantum ESPRESSO package [59,60] for first-principles electronic structure calculations of $Co_3Sn_2S_2$ within LDA and LSDA, which are performed using projector augmented waves (PAW) in the plane wave basis with spin-orbit coupling included. Scalar relativistic PAW pseudopotentials are employed, with exchange and correlation terms included through the Perdew-Burke-Ernzerhof (PBE) parametrization scheme as implemented in pslibrary21 [61]. The self-consistent calculation is performed using the experimental lattice constants [62], on a grid of $10 \times 10 \times 10$ $\boldsymbol{k}$ points with an energy cutoff of 60 Ry, and subsequently projected onto maximally localized Wannier functions using the WANNIER90 package [63], with a starting basis of Co-*3d*, Sn-*5sp*, and S-*3p* orbitals.

The resulting tight-binding Hamiltonian in the Wannier function basis is used to construct a 60-unit-cell slab for the surface state calculations. The supercell Hamiltonian is assembled along the [001] crystallographic direction and truncated along the Sn and S surfaces shown in Fig. 1. To isolate the surface states for comparison with ARPES spectra, we color the bands red(blue) at each k point proportionally to the probability density at the S (Sn) surface for their corresponding eigenvectors [Figs. 5(c) and 5(d)]. Several additional layers of atoms are included in our definition of the slab surface, to account for the long penetration depth of the surface states into the bulk [51], and to incorporate the contribution of the Co atoms, since the surface states for these terminations have primarily Co-3d character [64].

Numerical slab calculations of the S termination show numerous surface bands at the Γ point, which do not appear on the Sn terminated surface, motivating us to identify the spectrum in Fig. 5(b) with the S termination. Additionally, the calculation for the S surface shows a band in the gap between the two bulk states at K, which is also not present in the Sn termination. This is consistent with the filled-in spectral weight at $E_B \sim 300$ meV in Fig. 5(b) as compared to Fig. 5(a). This interpretation is also consistent with prior XPS studies, which associate the low-energy shoulder on the S-*2p* levels with surface S atoms, whose energy shift stems from reduced coordination at the surface [23,64]. The stronger shoulder in Fig. 4(b) vs 4(a) thus suggests a greater contribution from surface S atoms, and a predominant S termination on the sample position used for Figs. 4(b) and 5(b). We note that the spectra associated with different cleaves were observed with 80 μm photoemission spot size, which suggests that different cleave terminations typically have macroscopic dimensions, and in fact some of our experiments yielded only a single termination. We also acknowledge studies of nanoscale inhomogeneity within that macroscopic cleave termination [19,66], which our simplified model of a single termination does not consider.

IV. ELECTRONIC STRUCTURE CHANGES ACROSS T_c

To describe the physics of the magnetic transition and associated changes in the electronic structure, we present ARPES measurements of $Co_3Sn_2S_2$ across T_c, focusing on the high symmetry cut along $\Gamma - K$ in the 2D projected BZ shown in Fig. 1(b).

Figure 6 investigates the temperature dependence of low-energy electronic structure through T_c on the Sn termination. Example spectra are shown at 30 K ($T << T_c$), 100 K, 135 K, 177 K ($T = T_c$), and 205 K ($T \gg T_c$) in panels (a1)–(a5). Corresponding curvature plots [65] [Fig. 6(b)] highlight less visible features in the spectra, particularly the parabolic dispersion around Γ. Although this feature has lower cross section than other bands, it still yields a clear local maximum in the EDC [Fig. 6(c)] (and SM [54]).

In the energy and momentum range shown in Fig. 6 the predominant features observed are bulk bands, highlighted in red in panel (a1), and a surface-like band, which forms the Fermi arc, highlighted with a black-dashed line. The bulk and surface character of these respective features was established in prior photon-energy dependence studies [20]. These features are in qualitative agreement with calculations shown in Fig. 5, as discussed further in SM [54]. The band that forms the Fermi arc is largely unchanged at 100 K, but at 135 K, this feature is weakened and shifted towards the K point. At 177 K, it is no longer present.

The bulk bands are best visualized via the EDC local maximum, which also corresponds well with the dominant features in the curvature plots. Figures 6(c)–6(e) show EDCs at three characteristic momenta—$k_x = 0.2$ Å^{-1}, K point, and M point—to emphasize the robustness of the observed energy shifts at each momentum. Additionally, EDCs at the M point show clear high-energy shoulders above T_c, indicating persisting features of the magnetic state, identified as the lower Hubbard band.

Figure 6(f) shows EDC local maxima across the cut. The dispersions derived in this manner coincide at all measured temperatures below T_c, but are distinct from those measured above T_c. Intermediate behavior is shown at 177 K = T_c, both in the EDC local maxima and in the curvature plots. Above T_c, EDC local maxima are consistently shifted to lower binding energy, but the shift is nonmonotonic: At the Γ point, the shift is 150 meV, at the K point the shift is 70 meV, and at the M point the shift is 130 meV. Dispersions above T_c are significantly flatter than below T_c, indicating an enhanced effective mass relative to the ferromagnetic regime. This is demonstrated in Fig. 6(g) where a characteristic dispersion $T < T_c$ is compared to a characteristic dispersion $T > T_c$ in two different ways: Energy shift and renormalization. A simple shift does not reproduce the $T > T_c$ dispersion, but a renormalization by a factor of $\sim$3 produces a dispersion coincident with the one measured above T_c.

As we have already discussed, the ferromagnetism of $Co_3Sn_2S_2$ below T_c serves to split the electronic bands within the spin-majority and spin-minority channels [54], resulting in a band gap in the spin-minority states. One might naively attribute the apparent shift in the band structure observed by experiments solely to the disappearance of exchange splitting in this itinerant magnet. If the magnetic moments are presumed to disappear entirely, the state where exchange splitting vanishes could be represented using the electronic structure predicted by nonmagnetic LDA. Then, the behavior across the ferromagnetic-paramagnetic transition can be identified with the shift of the spin-majority band between magnetic LSDA and nonmagnetic LDA [22,23].

While it is tempting to compare the results of the nonmagnetic calculation with the behavior of $Co_3Sn_2S_2$ above T_c in this way, such an interpretation does not entirely capture the physics of the paramagnetic phase. The magnetism is only fully quenched at temperatures comparable to the band splitting of ∼0.5 eV, far above the melting point of the material. For experimentally relevant temperatures above T_c, ferromagnetism disappears due to the suppression of long-range order by temperature driven fluctuations. However, the persistence of local moments seen in the Curie Weiss susceptibility [54], suggests a more complex many-body behavior.

The microscopic picture of magnetism is usually considered in the limit of large, moderate, and small ratios of Coulomb interaction U to the electronic bandwidth W. When $U \gg W$, we are in the archetypal Mott regime where disorder can narrow the bands by further limiting intersite hopping, while $U << W$ corresponds to the standard itinerant state. However, when $U \sim W$, we recover a distinctive strongly correlated state, where renormalized quasiparticles in the vicinity of E_F and Hubbard band states at higher energies are simultaneously present.

Applying this interpretation of magnetic disorder to $Co_3Sn_2S_2$, it becomes clear that that the relative magnitudes of the bandwidth and band splitting will determine the behavior above T_c. For a large band splitting, magnetic disorder and associated correlations will simply serve to renormalize the width of the Hubbard bands. On the other hand, if $U \sim W$, the magnetic disorder at high T will lead to a narrow quasiparticle band, resulting in a correlated metallic state, appearing as a spectral shift in photoemission measurements [67].

The expected behavior can be estimated from the parameters of our extracted tight-binding model. The nearest-neighbor hopping parameter is approximately $t \sim 0.8$ eV, while a range of Hubbard U values $U \sim 2-4$ eV result in a reasonable exchange splitting between the bands. For the Co-$3d_{x^2-y^2}$ three band model at 5/6 filling, the highest occupied state (Fig. 3) renormalizes the Coulomb repulsion by a factor of three. Representing this system as a simplified single-band Hubbard model with a bandwidth $W \sim 0.8$ eV and effective $U_{\text{eff}} \sim 1.3$ eV, places it in the regime $U \sim 1.6W$, which is known to be very close to a Mott transition [68], although multi–orbital effects should affect the precise U/W ratio [69]. Thus, it is expected that $Co_3Sn_2S_2$ would transition to a correlated metallic state once the moments are disordered by temperature.

There are numerous signatures of correlations in $Co_3Sn_2S_2$, but a complete picture is only beginning to emerge. Even in the ferromagnetic phase there is a modest enhancement of the electronic mass, with the experimental Sommerfeld gamma $\gamma_{\text{expt}} = 9.8–10.8$ mJ mol^{-1} K^{-1} [15,70] exceeding the value computed from the electronic density of states $\gamma_{\text{th}} = 3.25$ mJ mol^{-1} K^{-1} [54] by a factor of ∼3. However, it should be noted that mass enhancement will be unequal across the bands, with correlation effects playing a more significant role in the renormalization of the magnetic Co-$3d_{x^2-y^2}$ band. In fact, the electronic-bandwidth renormalizations of Co-$3d_{xy}$ and Co-$3d_{x^2-y^2}$ are found to be strongest with increasing Coulomb energy [30], which is consistent with our description, as these are the orbitals that most align with the rotated Co-$3d_{x^2-y^2}$ orbitals in our symmetry-adapted basis. Further evidence for correlations comes from optical conductivity measurements, which show a moderate band renormalization that necessitates a rescaling of the computed spectrum by a factor of ∼0.68 – 0.76 to match experiment [22,30]. This is consistent with the recently measured ratio of 0.70 between experimental and theoretical bandwidths [20].

This wide assortment of correlated properties is further enriched by temperature and doping effects. A frustrated in-plane anti-ferromagnetic component emerges at a temperature $T_a \sim 90$ K, that tilts the Co magnetic moments [16,34], affecting the long-range correlations and resulting in a non-monotonic magnetoelastic response for temperatures between T_a and T_c [71]. As the temperature is raised through T_c, optical conductivity measurements also show a transfer of spectral weight to higher energy peaks [22], suggesting a complex magnetic transition. Doping with electrons or holes reveals additional anomalous behaviors. For instance hole doped $Co_3Sn_{2-x}In_xS_2$ displays a strong enhancement of the quadratic term in the electrical resistivity $\rho(T) = \rho_0 + AT^2$ near $x = 0.8$, implying an enhanced electronic mass due to the increased correlation effects [70]. Hole doping with iron leads to an improvement in the thermoelectric properties, which is associated with an enhanced density of states, while electron doping with nickel significantly decreases the resistivity, resulting in a more metallic state with increasing nickel content [72].

A moderate band renormalization by a factor of ∼0.7 would imply that most of the spectral weight resides not in the Hubbard bands, but in the quasiparticle band, which is consistent with the picture that emerges from our ARPES data shown in Fig. 6. However, a complete treatment of these effects would involve taking into account the three-Co cluster in a full-fledged many-body calculation [30]. Nevertheless, the magnetic transition from ferromagnet to correlated metal in $Co_3Sn_2S_2$, and the apparent shift of low energy bands seen in photoemission, can be understood using a DLM model [37]. We compute the electronic structure using LDA+DLM, as well as in the ferromagnetic LDA+U and nonmagnetic LDA settings. The Hubbard U parameter is selected semi-empirically by comparing the position of the flat $d_{x^2-y^2}$ band along $\Gamma - T$. A value of $U = 2$ eV places this band 0.3 eV below the Fermi level, which is consistent with photoemission measurements [23]. Alternatively, one can use the larger value of U and adjust the double counting to match with ARPES. The spectral functions $\mathcal{A}(\boldsymbol{k}, \omega) = \Im[G(\boldsymbol{k}, \omega)]$ for each calculation are shown in Fig. 7.

A comparison of the ferromagnetic and DLM calculations confirms the existence of a correlated regime, clearly showing the exchange split bands collapsing into one, with the DLM result nearly matching the dispersion of the Co-$d_{x^2-y^2}$ band in the nonmagnetic calculation. This is an interesting result because the DLM calculation would naively be expected to produce only Hubbard bands and should not differ much from the magnetically ordered LDA+U spectrum. However, the important effect of the DMFT self-consistency included in the coherent potential approximation (CPA), results in the appearance of a quasiparticle band, which is seen to be significantly broadened due to quasiparticle life time effects. Experimentally, this would present as an apparent shift of spectral weight closer to E_F, exactly as seen by ARPES measurements. We stress that despite the visual similarity between the LDA+DLM and nonmagnetic LDA spectral functions, the paramagnetic state we model with DLMs is indeed a complex strongly correlated many-body state, and whose band narrow-

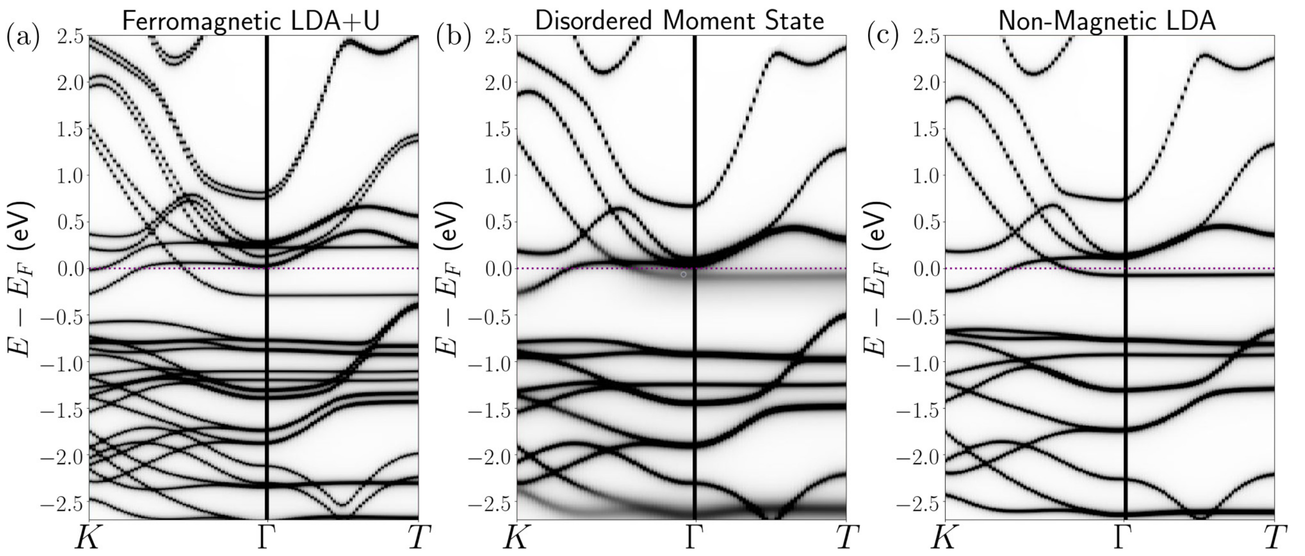

FIG. 7. Plots of the momentum-resolved spectral function $\mathcal{A}(\boldsymbol{k}, \omega) = \Im[G(\boldsymbol{k}, \omega)]$ along $K - \Gamma - T$. The spectral functions for (a) ferromagnetic LDA+U, (b) LDA+DLM, and (c) nonmagnetic LDA are shown.

ing effect cannot be fully captured by our CPA-based DLM method, nor by single-site DMFT calculations as reported earlier [30].

V. WEYL PHYSICS ACROSS T$_c$

As the temperature is raised through T_c, besides an effective shift in the observed spectral density, the vanishing ferromagnetism also removes the global $\mathcal{T}$-breaking symmetry. Above T_c the system has both $\mathcal{I}$ and $\mathcal{T}$ symmetries, meaning any Weyl points in the ferromagnetic state can no longer exist.

Figure 8 compares photoemission data for the Sn termination across T_c with the results of numerical calculations. The ARPES constant energy maps shown in Figs. 8(a) and 8(b) are overlaid with constant energy slices of the bands computed for the slab geometry using the Wannier–basis Hamiltonian extracted from LSDA. These Fermi surface contours are colored based on the probability density contribution at each $\boldsymbol{k}$ point; red for the S surface and blue for Sn, as indicated by the corresponding planes in Fig. 1.

For the ferromagnetic calculation [Fig. 8(a)], the computed states have strong contributions from the Sn surface that form petal-like triangular features at the corners of the two-dimensional BZ, which match well with the dark regions of high spectral density seen in the ARPES data. The reason for the apparent six-fold rotational symmetry in both theory and experiment, is that ferromagnetism breaks the $\boldsymbol{k} \leftrightarrow -\boldsymbol{k}$ symmetry along the k_z direction, which is effectively integrated out for these data, meaning deviations from six-fold symmetry are very slight. Specifically, there is a small anisotropy in the theory calculation between K and K' corners at opposite momenta, consistent with the C_3 rotational symmetry.

Above the transition temperature, the Fermi surface looks markedly different [Fig. 8(b)]. In the photoemission data, there is a blurring of spectral details stemming from the expected magnetic disorder and fluctuations. Simultaneously, the absence of $\mathcal{T}$-breaking terms in the nonmagnetic theory calculation manifests as a six-fold rotational symmetry of the contours, along with a near total absence of surface state contributions at E_F.

As the energy is raised above E_F in the ferromagnetic calculation [Fig. 8(e)], the constant-energy slices reveal the topological nature of the surface states. The blue (Sn) surface states pull away from the M points of the BZ with increasing energy, and the three trivial surface states merge with the bulk and vanish. The remaining three Sn surface states connect with the six Weyl cone projections, located near the M points along the $\Gamma - M$ lines, and form topological Fermi arcs as shown in Fig. 8(e). To explicitly demonstrate the connection between the Fermi surface and topological Fermi arc states just above E_F, in our Supplemental Material we provide an animation of the slab calculation over a range of energies [54].

Having discussed the changes in fermiology across T_c, we now examine the details of the bands, which form the Weyl cones. We inspect the cut in the k_x direction midway between $K - \Gamma - K'$ and the BZ edge, marked by black lines in Figs. 8(a) and 8(b). This cut passes through the M points of the BZ, and crosses the Weyl cones of the two topological points on either side [Figs. 8(c) and 8(d)]. The ferromagnetic LSDA band structure shown in green highlights the two pairs of conical bands that rise upward towards the Fermi energy to form the Weyl cones, similarly to those seen in prior photoemission measurements [20]. While the band connecting the cones in each pair is located above E_F and is not directly visible in the presented ARPES data, the occupied sides of the conical features are clearly visible to the left and right of $k_x = 0$ in the photoemission data [Fig. 8(c)]. Above T_c, the occupied side of the cone-like features are nearly absent from ARPES data, consistent with the LDA+DLM calculation [Fig. 8(f)], which shows the correlated state just above E_F. The faint spectral features visible near $k_x \sim 0$ and $k_x \sim 1.1$ Å^{-1} around -0.3 eV in the photoemission spectra can be explained as the remnants of the lower Hubbard that have not entirely disappeared due to the surviving local magnetic order. This

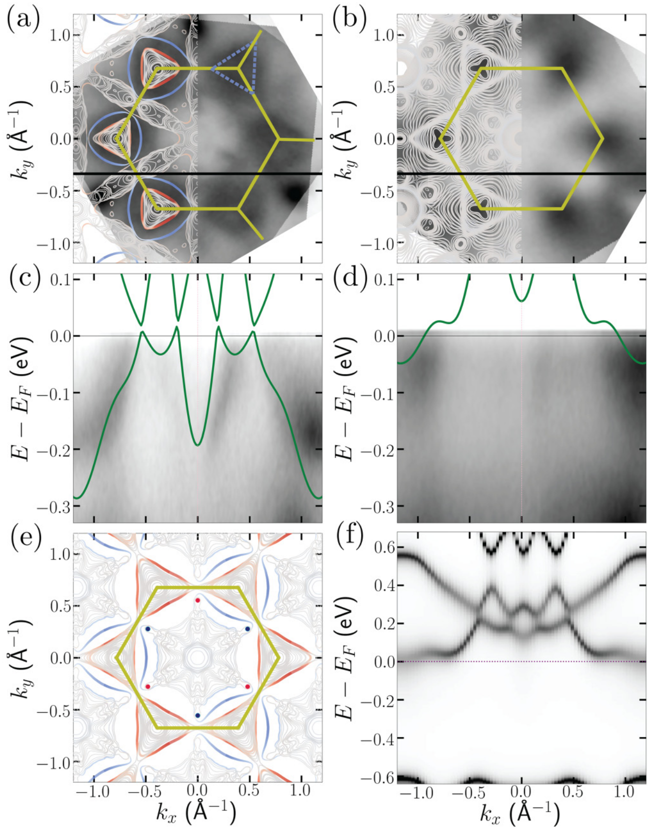

FIG. 8. ARPES spectra below and above T_c with computed overlays. Constant energy maps of ARPES spectra at $E = E_F$ below T_c ($T = 30$ K) (a), and above T_c ($T = 200$ K) (b), overlaid with the Fermi surface contours for the ferromagnetic (a) and nonmagnetic (b) slab calculation. Blue-dashed lines highlight the location of Fermi arcs in the first and second BZ. For the cuts indicated by the horizontal black lines in (a) and (b), the band structure is shown in (c) and (d). The Weyl cones visible in (c) disappear above T_c (d). Band structure calculations for the ferromagnetic (c) and nonmagnetic (d) regimes are overlaid for comparison. (e) Fermi surface contours computed at the Weyl energy. (f) The band structure computed with LDA+DLM.

is consistent with evidence for the persistence of the lower Hubbard band presented in Fig. 6(e).

The annihilation of bulk Weyl nodes should be accompanied by changes in the Fermi arcs that ultimately also lead to their disappearance. The Fermi arc features are most clearly seen in the second BZ and are indeed absent above T_c. The Γ-K cut in Fig. 6 also cuts through the band that has been identified as the one forming the Fermi arc [20], and shows a finer temperature-dependence. The band that forms the Fermi arc shifts to momenta closer to K by 135 K, and is absent at T_c.

VI. CONCLUSIONS AND OUTLOOK

In this paper, we have shown how the half-metallic ferromagnetism of $Co_3Sn_2S_2$ emerges in the partially filled Co-3$d_{x^2-y^2}$ band crossing E_F. The critical physics develops on the cluster of Co atoms, for which the highest occupied half-filled state creates a resonance, which renormalizes the Coulomb interaction to one-third of its nominal value. The comparable energy scales of bandwidth and interactions result in a strongly correlated magnetic state. As the temperature is raised above T_c, the system undergoes a transformation where long range order disappears and the Zeeman-split bands merge into one, transitioning from a Mott ferromagnet to correlated metal.

The details of the magnetism in this material are highly relevant to its topological properties. However, investigations of this topology in the context of bulk-boundary correspondence need to consider the variety of possible surface terminations in this material and associated differences in surface band structure. The spectroscopic characterization presented here identifies key features that are distinct for the S and Sn terminations, and can be used to differentiate these surfaces. Characteristic signatures of the different surface terminations will be valuable in future experiments, which are needed to understand further the various aspects related to the disappearance of topology, including the role of magnetic domains, local magnetic correlations, and vanishing topological Fermi arcs across the magnetic transition.

The ferromagnetism in $Co_3Sn_2S_2$ breaks $\mathcal{T}$ symmetry and is a necessary prerequisite for the existence of topological Weyl points. The strongly correlated metallic state in $Co_3Sn_2S_2$ emerges as a result of magnetic disorder at higher temperatures, restoring $\mathcal{T}$ symmetry and precluding the existence of topology. The detailed behavior of magnetic fluctuations has an effect on topology not just above T_c, but throughout a wide temperature range approaching the transition. In this way the topological properties and strong correlations in this system are intricately linked, and one cannot be adequately considered without the other. Naively, the Weyl points exist as a result of broken time-reversal symmetry, and should annihilate when the magnetism breaking this symmetry vanishes. However, in the present system, magnetism goes away gradually with temperature as spin-fluctuations increase and the local moments become disordered. This process breaks the local translation symmetry of the crystal, which is necessary for Weyl points to exist. As such, it is not yet clear whether the Weyl points explicitly annihilate or simply cease to exist when the underlying translation symmetry is broken. This is an important point for future studies to clarify.

During the review process, two other papers [73,74], which examine the topological features in $Co_3Sn_2S_2$ across T_c were uploaded to arXiv.

ACKNOWLEDGMENTS

The authors acknowledge helpful discussions with E. H. da Silva Neto and Matthew Staab. I.M.V. and A.R. acknowledge support from UC Davis Startup funds and the Alfred P. Sloan Foundation (Grant No. FG-2019-12170). Theoretical work by V.I. and S.S. was supported by NSF DMR Grant No. 1832728. V.T. and Z.S. acknowledge support from the UC Lab Fees Research Program (LFR-20-653926) and UC Davis Startup funds. This research used resources of the Advanced Light Source, a U.S. DOE Office of Science User Facility, under Contract No. DE-AC02-05CH11231.

[1] B. Keimer and J. E. Moore, Nat. Phys. **13**, 1045 (2017).

[2] Y. Tokura, M. Kawasaki, and N. Nagaosa, Nat. Phys. **13**, 1056 (2017).

[3] X. Wan, A. M. Turner, A. Vishwanath, and S. Y. Savrasov, Phys. Rev. B **83**, 205101 (2011).

[4] G. Xu, H. Weng, Z. Wang, X. Dai, and Z. Fang, Phys. Rev. Lett. **107**, 186806 (2011).

[5] I. Belopolski, K. Manna, D. S. Sanchez, G. Chang, B. Ernst, J. Yin, S. S. Zhang, T. Cochran, N. Shumiya, H. Zheng *et al.*, Science **365**, 1278 (2019).

[6] Z. Cai, S. Bao, W. Wang, Z. Ma, Z.-Y. Dong, Y. Shangguan, J. Wang, K. Ran, S. Li, K. Kamazawa, M. Nakamura, D. Adroja, S.-L. Yu, J.-X. Li, and J. Wen, Phys. Rev. B **101**, 134408 (2020).

[7] G. Chang, B. Singh, S.-Y. Xu, G. Bian, S.-M. Huang, C.-H. Hsu, I. Belopolski, N. Alidoust, D. S. Sanchez, H. Zheng, H. Lu, X. Zhang, Y. Bian, T.-R. Chang, H.-T. Jeng, A. Bansil, H. Hsu, S. Jia, T. Neupert, H. Lin *et al.*, Phys. Rev. B **97**, 041104(R) (2018).

[8] K. Kuroda, T. Tomita, M. T. Suzuki, C. Bareille, A. A. Nugroho, P. Goswami, M. Ochi, M. Ikhlas, M. Nakayama, S. Akebi *et al.*, Nat. Mater. **16**, 1090 (2017).

[9] K. Takiguchi, Y. K. Wakabayashi, H. Irie, Y. Krockenberger, T. Otsuka, H. Sawada, S. A. Nikolaev, H. Das, M. Tanaka, Y. Taniyasu, and H. Yamamoto, Nat. Commun. **11**, 4969 (2020).

[10] N. P. Armitage, E. J. Mele, and A. Vishwanath, Rev. Mod. Phys. **90**, 015001 (2018).

[11] T. O. Wehling, A. M. Black-Schaffer, and A. V. Balatsky, Adv. Phys. **63**, 1 (2014).

[12] B. Yan and C. Felser, Annu. Rev. Condens. Matter Phys. **8**, 337 (2017).

[13] H. Nielsen and M. Ninomiya, Phys. Lett. B **130**, 389 (1983).

[14] T. Kubodera, H. Okabe, Y. Kamihara, and M. Matoba, Phys. B: Condens. Matter **378-380**, 1142 (2006).

[15] W. Schnelle, A. Leithe-Jasper, H. Rosner, F. M. Schappacher, R. Pöttgen, F. Pielnhofer, and R. Weihrich, Phys. Rev. B **88**, 144404 (2013).

[16] E. Liu, Y. Sun, N. Kumar, L. Muechler, A. Sun, L. Jiao, S.-Y. Yang, D. Liu, A. Liang, Q. Xu *et al.*, Nat. Phys. **14**, 1125 (2018).

[17] S. Li, G. Gu, E. Liu, P. Cheng, B. Feng, Y. Li, L. Chen, and K. Wu, ACS Appl. Electron. Mater. **2**, 126 (2020).

[18] Y. Okamura, S. Minami, Y. Kato, Y. Fujishiro, Y. Kaneko, J. Ikeda, J. Muramoto, R. Kaneko, K. Ueda, V. Kocsis *et al.*, Nat. Commun. **11**, 4619 (2020).

[19] N. Morali, R. Batabyal, P. K. Nag, E. Liu, Q. Xu, Y. Sun, B. Yan, C. Felser, N. Avraham, and H. Beidenkopf, Science **365**, 1286 (2019).

[20] D. F. Liu, A. J. Liang, E. K. Liu, Q. N. Xu, Y. W. Li, C. Chen, D. Pei, W. J. Shi, S. K. Mo, P. Dudin *et al.*, Science **365**, 1282 (2019).

[21] L. Jiao, Q. Xu, Y. Cheon, Y. Sun, C. Felser, E. Liu, and S. Wirth, Phys. Rev. B **99**, 245158 (2019)

[22] R. Yang, T. Zhang, L. Zhou, Y. Dai, Z. Liao, H. Weng, and X. Qiu, Phys. Rev. Lett. **124**, 077403 (2020).

[23] M. Holder, Y. S. Dedkov, A. Kade, H. Rosner, W. Schnelle, A. Leithe-Jasper, R. Weihrich, and S. L. Molodtsov, Phys. Rev. B **79**, 205116 (2009).

[24] W. Shi, L. Muechler, K. Manna, Y. Zhang, K. Koepernik, R. Car, J. van den Brink, C. Felser, and Y. Sun, Phys. Rev. B **97**, 060406(R) (2018).

[25] Q. Wang, Y. Xu, R. Lou, Z. Liu, M. Li, Y. Huang, D. Shen, H. Weng, S. Wang, and H. Lei, Nat. Commun. **9**, 3681 (2018).

[26] G. S. Thakur, P. Vir, S. N. Guin, C. Shekhar, R. Weihrich, Y. Sun, N. Kumar, and C. Felser, Chem. Mater. **32**, 1612 (2020).

[27] S. N. Guin, P. Vir, Y. Zhang, N. Kumar, S. J. Watzman, C. Fu, E. Liu, K. Manna, W. Schnelle, J. Gooth *et al.*, Adv. Mater. **31**, 1806622 (2019).

[28] A. Sakai, Y. P. Mizuta, A. A. Nugroho, R. Sihombing, T. Koretsune, M.-T. Suzuki, N. Takemori, R. Ishii, D. Nishio-Hamane, R. Arita *et al.*, Nat. Phys. **14**, 1119 (2018).

[29] T. Asaba, V. Ivanov, S. M. Thomas, S. Y. Savrasov, J. D. Thompson, E. D. Bauer, and F. Ronning, Sci. Adv. **7**, abf1467 (2021).

[30] Y. Xu, J. Zhao, C. Yi, Q. Wang, Q. Yin, Y. Wang, X. Hu, L. Wang, E. Liu, G. Xu *et al.*, Nat. Commun. **11**, 3985 (2020).

[31] C. Lee, P. Vir, K. Manna, C. Shekhar, J. E. Moore, M. A. Kastner, C. Felser, and J. Orenstein, arXiv:2104.13381.

[32] M. A. Kassem, Y. Tabata, T. Waki, and H. Nakamura, Phys. Rev. B **96**, 014429 (2017).

[33] E. Lachman, R. A. Murphy, N. Maksimovic, R. Kealhofer, S. Haley, R. D. McDonald, J. R. Long, and J. G. Analytis, Nat. Commun. **11**, 560 (2020).

[34] Z. Guguchia, J. A. T. Verezhak, D. J. Gawryluk, S. S. Tsirkin, J.-X. Yin, I. Belopolski, H. Zhou, G. Simutis, S.-S. Zhang, T. A. Cochran *et al.*, Nat. Commun. **11**, 559 (2020).

[35] G. Zheng, X. Zhu, Y. Liu, J. Lu, W. Ning, H. Zhang, W. Gao, Y. Han, J. Yang, H. Du, K. Yang, Y. Zhang, and M. Tian, Phys. Rev. B **96**, 121401(R) (2017).

[36] S.-Y. Gao, S. Xu, H. Li, C.-J. Yi, S.-M. Nie, Z.-C. Rao, H. Wang, Q.-X. Hu, X.-Z. Chen, W.-H. Fan, J.-R. Huang, Y.-B. Huang, N. Pryds, M. Shi, Z.-J. Wang, Y.-G. Shi, T.-L. Xia, T. Qian, and H. Ding, Phys. Rev. X **11**, 021016 (2021).

[37] A. J. Pindor, J. Staunton, G. M. Stocks, and H. Winter, J. Phys. F **13**, 979 (1983).

[38] R. Weihrich, I. Anusca, and M. Zabel, Z. Anorg. Allg. Chem. **631**, 1463 (2005).

[39] R. Weihrich and I. Anusca, Z. Anorg. Allg. Chem. **632**, 1531 (2006).

[40] X. Lin, S. L. Bud'ko, and P. C. Canfield, Philos. Mag. **92**, 2436 (2012).

[41] M. A. Kassem, Y. Tabata, T. Waki, and H. Nakamura, J. Cryst. Growth **426**, 208 (2015).

[42] V. Nagpal and S. Patnaik, J. Phys.: Condens. Matter **32**, 405602 (2020).

[43] R. Weihrich, W. Yan, J. Rothballer, P. Peter, S. M. Rommel, S. Haumann, F. Winter, C. Schwickert, and R. Pöttgen, Dalton Trans. **44**, 15855 (2015).

[44] Y. Sakai, R. Tanakadate, M. Matoba, I. Yamada, N. Nishiyama, T. Irifune, K. Funakoshi, T. Kunimoto, Y. Higo, and Y. Kamihara, J. Phys. Soc. Jpn. **84**, 044705 (2015).

[45] J.-X. Yin, S. S. Zhang, G. Chang, Q. Wang, S. S. Tsirkin, Z. Guguchia, B. Lian, H. Zhou, K. Jiang, I. Belopolski *et al.*, Nat. Phys. **15**, 443 (2019).

[46] M. A. Kassem, Y. Tabata, T. Waki, and H. Nakamura, J. Phys.: Condens. Matter **33**, 015801 (2020).

[47] Y. S. Dedkov, M. Holder, S. L. Molodtsov, and H. Rosner, J. Phys.: Conf. Ser. **100**, 072011 (2008).

[48] A. Ozawa and K. Nomura, J. Phys. Soc. Jpn. **88**, 123703 (2019).

[49] W. Luo, Y. Nakamura, J. Park, and M. Yoon, npj Comput. Mater. **7**, 2 (2021).

[50] F. Pielnhofer, J. Rothballer, P. Peter, W. Yan, F. M. Schappacher, R. Pöttgen, and R. Weihrich, Z. Anorg. Allg. Chem. **640**, 286 (2014).

[51] Q. Xu, E. Liu, W. Shi, L. Muechler, J. Gayles, C. Felser, and Y. Sun, Phys. Rev. B **97**, 235416 (2018).

[52] S. Y. Savrasov, Phys. Rev. B **54**, 16470 (1996).

[53] S. Y. Savrasov and D. Y. Savrasov, Phys. Rev. B **46**, 12181 (1992).

[54] The Supplemental Material at http://link.aps.org/supplemental/10.1103/PhysRevB.104.155115 for further theoretical and experimental details as well as a video showing the evolution of surface states as energy is increased.

[55] K. Haule, Phys. Rev. B **75**, 155113 (2007).

[56] A. Rossi, G. Resta, S. H. Lee, R. D. Redwing, C. Jozwiak, A. Bostwick, E. Rotenberg, S. Y. Savrasov, and I. M. Vishik, Phys. Rev. B **102**, 121110(R) (2020).

[57] Y. Xing, J. Shen, H. Chen, L. Huang, Y. Gao, Q. Zheng, Y.-Y. Zhang, G. Li, B. Hu, G. Qian *et al.*, Nat. Commun. **11**, 5613 (2020).

[58] Y. Gao, X. Jin, Y. Gao, Y.-Y. Zhang, and S. Du, Chin. Phys. B **30**, 077102 (2021).

[59] P. Giannozzi, O. Andreussi, T. Brumme, O. Bunau, M. B. Nardelli, M. Calandra, R. Car, C. Cavazzoni, D. Ceresoli, M. Cococcioni *et al.*, J. Phys.: Condens. Matter **29**, 465901 (2017).

[60] P. Giannozzi, S. Baroni, N. Bonini, M. Calandra, R. Car, C. Cavazzoni, D. Ceresoli, G. L. Chiarotti, M. Cococcioni, I. Dabo *et al.*, J. Phys.: Condens. Matter **21**, 395502 (2009).

[61] A. Dal Corso, Comput. Mater. Sci. **95**, 337 (2014).

[62] P. Vaqueiro and G. G. Sobany, Solid State Sci. **11**, 513 (2009).

[63] A. A. Mostofi, J. R. Yates, Y.-S. Lee, I. Souza, D. Vanderbilt, and N. Marzari, Comput. Phys. Commun. **178**, 685 (2008).

[64] G. Li, Q. Xu, W. Shi, C. Fu, L. Jiao, M. E. Kamminga, M. Yu, H. Tüysüz, N. Kumar, V. Süß *et al.*, Sci. Adv. **5**, aaw9867 (2019).

[65] P. Zhang, P. Richard, T. Qian, Y.-M. Xu, X. Dai, and H. Ding, Rev. Sci. Instrum. **82**, 043712 (2011).

[66] K. M. Roccapriore, Q. Zou, L. Zhang, R. Xue, J. Yan, M. Ziatdinov, M. Fu, D. Mandrus, M. Yoon, B. Sumpter, Z. Gai, and S. V. Kalinin, ACS Nano **15**, 11806 (2021).

[67] M. J. Rozenberg, G. Kotliar, and H. Kajueter, Phys. Rev. B **54**, 8452 (1996).

[68] A. Georges, G. Kotliar, W. Krauth, and M. J. Rozenberg, Rev. Mod. Phys. **68**, 13 (1996).

[69] S. Florens, A. Georges, G. Kotliar, and O. Parcollet, Phys. Rev. B **66**, 205102 (2002).

[70] M. A. A. A. Kassem, Ph.D. thesis, Kyoto University, 2017.

[71] C. Liu, C. Yi, X. Wang, J. Shen, T. Xie, L. Yang, T. Fennel, U. Stuhr, S. Li, H. Weng, Y. Shi, E. Liu, and H. Luo, Sci. China: Phys., Mech. Astron. **64**, 257511 (2021).

[72] P. Mangelis, P. Vaqueiro, J.-C. Jumas, I. da Silva, R. I. Smith, and A. V. Powell, J. Solid State Chem. **251**, 204 (2017).

[73] I. Belopolski, T. A. Cochran, X. Liu, Z.-J. Cheng, X. P. Yang, Z. Guguchia, S. S. Tsirkin, J.-X. Yin, P. Vir, G. S. Thakur *et al.*, arXiv:2105.14034.

[74] D. F. Liu, Q. N. Xu, E. K. Liu, J. L. Shen, C. C. Le, Y. W. Li, D. Pei, A. J. Liang, P. Dudin, T. K. Kim *et al.*, arXiv:2106.03229.

Correction: A sentence that previously appeared as the sixth sentence in the abstract was a partial duplication of the following sentence and has been removed.